

# Supplemental Materials: Quantum nano-cavity optics with configurable nano-tips

Molly A. May,<sup>1</sup> Tong Wu,<sup>3</sup> David Fialkow,<sup>2</sup> Kyoung-Duck Park,<sup>4</sup>

Jaron A. Kropp,<sup>2</sup> Theodosia Gougousi,<sup>2</sup> Philippe Lalanne,<sup>3</sup>

Matthew Pelton,<sup>2\*</sup> Markus B. Raschke<sup>1\*</sup>

<sup>1</sup>Department of Physics, Department of Chemistry, and JILA, University of Colorado  
2000 Colorado Ave., Boulder, CO 80309, USA

<sup>2</sup>Department of Physics, UMBC (University of Maryland, Baltimore County),  
Baltimore, MD 22150, USA

<sup>3</sup>LP2N, Institute d'Optique, CNRS, Univ. Bordeaux  
Institut d'Optique, IOGS, France

<sup>4</sup>Department of Physics, School of Natural Sciences, Ulsan National Institute of Science and Technology  
50 UNIST-gil, Eonyang-eup, Ulsu-gun, Ulsan, South Korea

\*To whom correspondence should be addressed;

E-mail: markus.raschke@colorado.edu (M.B.R.), mpelton@umbc.edu (M.P.)

(Dated: 09/27/2019)

## I. SAMPLE PREPARATION

8-nm CdSe/ZnS QDs (900249-1ML, Sigma Aldrich), stabilized with octadecylamine ligands in toluene, were drop casted on an Au film coated with Al<sub>2</sub>O<sub>3</sub> after diluting the stock solution by a factor of 20,000. From AFM imaging, we verified that the density of the QDs on the surface was  $\sim 5$  dots in a  $1 \mu\text{m}$  by  $1 \mu\text{m}$  window and that they were well dispersed. Atomic layer deposition (ALD) was used to deposit the base and capping layers of Al<sub>2</sub>O<sub>3</sub> using trimethylaluminum (TMA) and water as precursors. Depositions were performed in a custom-built flow tube reactor. The base layers were deposited at 200 °C while the capping layers were deposited at 80 °C to avoid thermal degradation of the QDs. Depositions occurred under a steady flow of N<sub>2</sub>. Each ALD cycle consists of 0.1 s of TMA pulse, 30 s of N<sub>2</sub> purge, 0.5 s of water pulse, and 30 s of N<sub>2</sub> purge. The growth rate of Al<sub>2</sub>O<sub>3</sub> is  $\sim 0.1$  nm/cycle at 200 °C, and  $\sim 0.08$  nm/cycle at 80 °C. The number of ALD cycles was adjusted accordingly to achieve the desired dielectric film thickness. The film thickness was confirmed via spectroscopic ellipsometry (alpha-SE, J.A. Woollam) measurements on companion Si wafers.

## II. TIP-ENHANCED PHOTOLUMINESCENCE SPECTROSCOPY

In the TEPL spectroscopy setup, the sample was mounted to a piezoelectric transducer (PZT, P-611.3, Physik Instrumente) with sub-nm precision positioning below a mechanically driven and electrically controlled quartz tuning fork (resonance frequency = 32 kHz), which was used to regulate the tip-sample distance using the AFM shear-force frequency feedback [1]. Electrochemically etched Au tips ( $\sim 5 - 10$  nm apex radius) were attached to the tuning fork and coarsely positioned using a stepper motor (MX25, Mechonics AG), and shear-force feedback and sample positioning were controlled by a digital AFM controller (R9, RHK Technology). The sample was mounted at a  $35^\circ$  angle to the tip axis to maximize the electric field confinement [2]. Excitation was provided by a helium-neon laser beam (632.8 nm,  $\leq 1$  mW), providing a maximum fluence of  $10^9$  W/cm<sup>2</sup> to the near-field excitation region, with a half wave plate for polarization control that was focused onto the tip-sample interface using an objective lens (NA=0.8, LMPLFLN100 $\times$ , Olympus). Photoluminescence signal was collected in a backscattering geometry, passed through a dichroic mirror with a 633 nm cut-off and sent to a spectrometer ( $f = 500$  mm, SpectraPro 500i, Princeton Instruments) with a thermoelectrically cooled, electron-multiplied, charge-coupled device (CCD, ProEM+: 1600 eXcelon3, Princeton Instruments). The spectrometer was calibrated using a hydrogen mercury lamp and a 150 g/mm grating blazed for 800 nm is used to provide high bandwidth spectral information.

It is also worth noting that during TEPL measurements, the quantum dots exhibit significant blinking on a timescale of seconds in both the strong coupling and uncoupled regimes. While the photon count rates in TEPL experiments generally increase as the tip-sample distance decreases due to near-field enhancement of the PL signal as the tip is brought in line with the QD, significant blinking of the QD on the experimental timescale limits the ability to probe this and possibly more interesting effects in these experiments.

### III. MODELS FOR PLEXITON SPECTRA

The model used for fitting the TEPL spectra (Fig. 1, Fig. 2, and Fig. 3) is derived in Ref. [3] by starting from the interaction Hamiltonian for a quantized radiation field interacting with a two-level emitter located at the antinode of the field in an optical microcavity (the Jaynes-Cummings Hamiltonian) and allowing decay of both the field and the plasmon to thermal reservoirs in the Heisenberg-Langevin formalism. The rotating wave approximation is applied, and the evolution of the probability amplitudes for each possible state with one excitation in the system are obtained using the Weisskopf-Wigner approximation, which assumes that the state vector of the reservoir does not depend on its state at previous times. Finally, assuming that the emitter is prepared in an excited state at time  $t = 0$  and using the Weiner-Khintchine theorem yields Eq. 5 of the main text for the radiation spectrum of the emitter.

The upper- and lower-polariton frequencies can be found by diagonalizing the Hamiltonian, yielding

$$\omega_{\pm} = \frac{\omega_{\text{QD}} + \omega_{\text{spp}}}{2} - \frac{i}{4}(\gamma_{\text{QD}} + \gamma_{\text{spp}}) \pm \sqrt{(g/2)^2 + \frac{1}{4}\left(\omega_{\text{spp}} - \omega_{\text{QD}} - i\frac{\gamma_{\text{QD}} - \gamma_{\text{spp}}}{2}\right)^2} \quad (1)$$

This same expression can also be obtained by treating the cavity-emitter system as a pair of coupled, damped harmonic oscillators [4]. This same coupled-oscillator model can be used to obtain an analytical formula for the scattering spectrum  $\mu_{\text{PL}}$  of the coupled cavity-emitter system for a steady-state driving force at frequency  $\omega$ :

$$\mu_{\text{PL}} = \frac{F_0(\omega_{\text{QD}}^2 - \omega^2 - i\omega\gamma_{\text{QD}})}{(\omega_{\text{QD}}^2 - \omega^2 - i\omega\gamma_{\text{QD}})(\omega_{\text{spp}}^2 - \omega^2 - i\omega\gamma_{\text{spp}}) - \omega_{\text{QD}}\omega_{\text{spp}}g^2} \quad (2)$$

where  $F_0 = 4\omega_{\text{spp}}d_{\text{spp}}^2\mathbf{E}$  for plasmon dipole moment  $d_{\text{spp}}$  and electric field  $\mathbf{E}$ . In this case the scattering cross section  $\sigma_{\text{scatt}}$  is given by

$$\sigma_{\text{scatt}}(\omega) \propto \omega^4 |\mu_{\text{PL}}|^2. \quad (3)$$

#### IV. AGGREGATED ANTICROSSING DATA

Examples of anticrossing behavior for 72 individual QDs measured with three plasmonic cavities with intrinsic resonances ranging from  $\omega_{SP} = 1.83$  eV to  $\omega_{SP} = 1.85$  are shown in Fig. S1 in green, blue, and black, respectively. The  $|UP\rangle$  and  $|LP\rangle$  resonance energies for each cavity were averaged to generate the plot in Fig. 2(c) of the main text.

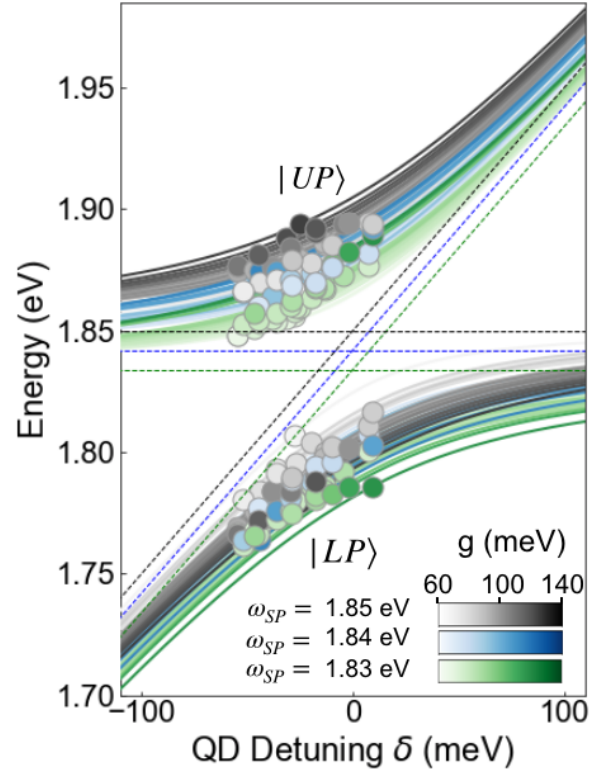


FIG. S1. **Anticrossing along three dimensions.** Spectral dispersion of QDs measured with three different plasmonic cavities with increasing plasmon resonance energy shown in green, blue, and black, respectively. Coupling strength is represented by the color bars, as shown in the inset.

#### IV. LATERAL LINE SCAN DATA

The spectral evolution and coupling strength as shown in Fig. 3 of the main text was also recorded for lateral scanning along the y-axis. This scan direction showed no measurable difference from that of the x-axis as shown in Fig. S2.

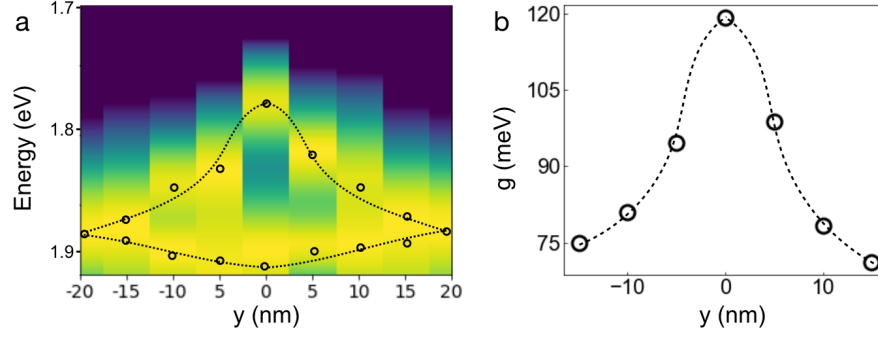


FIG. S2. **Lateral scan on y-axis.** Spectral evolution (a) and change in coupling strength (b) as the tip-QD position is scanned along the y-axis.

## V. FINITE-ELEMENT SIMULATION OF STRONG COUPLING

Finite-element simulations of the plexciton scattering spectra were performed using the wave-optics module in COMSOL. These simulations explicitly take into account the realistic geometry of the tip, QD, substrate, and capping layer. The tip was represented as a truncated cone with a hemispherical end. The opening angle of the tip was taken to be  $15^\circ$ , based on the SEM image of a tip with representative geometry, as shown in Fig. S3. The radius of curvature of the end of the tip was taken to be 10 nm, based on previous characterization of similar tips. The diameter of the QD was taken to be 8.4 nm, and the thickness of the aluminum oxide capper layer was taken to be 1 nm. Furthermore, in these simulations, the substrate is represented as having a finite size, and the tip is represented as having a finite length. Although these finite-size effects produce some changes in the calculated spectra, they do not significantly affect the results reported in the main text, because the optical fields are nearly entirely localized within the gap between the end of the tip and the substrate. For lateral displacement of the tip, the tip-sample separation was kept fixed at 2 nm. The incident field was polarized in the vertical direction (normal to the substrate). For the QD, the dielectric constant is taken to be a Lorentzian [5], with  $\epsilon_\infty = 5$ , resonance frequency  $\omega_o = 1.828$  eV, linewidth  $\gamma_o = 0.04$  eV, and oscillator strength and  $f = 1.0$ . The gold dielectric function is obtained by fitting data from Rakic et al [6] to a Lorentz-Drude model.

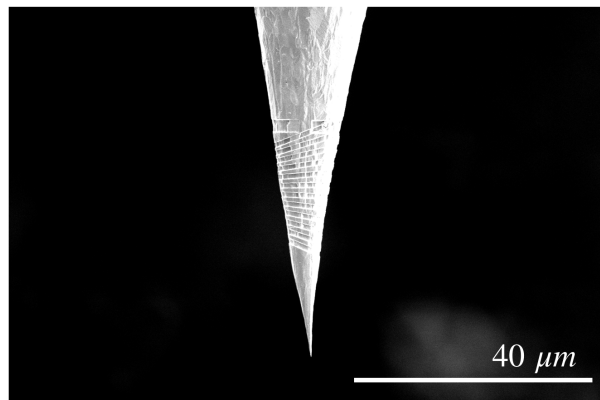


FIG. S3. **SEM image of tip.** SEM image of tip used to calculate the opening angle for FEM simulations.

The simulations are done in two parts. First, the background field is calculated by simulating the system without the gold tip or the QD (i.e., just the substrate). Next, the total field is calculated with all elements present. The scattered field is obtained by subtracting the results of the first calculation from the results of the second calculation. The simulated spectra were fit to Eq. 2, above, in order to obtain the coupling strength,  $g$ .

## VI. QUASINORMAL-MODE CALCULATIONS

For our tip cavity, the plasmon mode suffers from strong absorption and leakage and is no longer a stationary pattern as in a lossless cavity. It possesses a complex frequency,  $\tilde{\omega}_{\text{spp}} = \Omega_{\text{spp}} - i\Gamma_{\text{spp}}/2$ , and its electric field  $\tilde{\mathbf{E}}_{\text{spp}}(\mathbf{r})$ , defined as the eigenvector of the non-Hermitian Maxwell operator, possesses a phase factor that depends on  $\mathbf{r}$ , which is not encountered in the stationary patterns of lossless cavity modes. To take into account the additional phase factor, the real mode volume of conventional resonators should be abandoned and replaced by a complex number that takes into account the phase factor at the position of the oscillator [7]:

$$\tilde{V} = \frac{1}{2\epsilon_0 n^2 [\tilde{\mathbf{E}}_{\text{spp}}(r_e) \cdot \mathbf{u}]^2} \quad (4)$$

where  $\mathbf{u}$  is a unit vector denoting the orientation of the electric-dipole moment of the QD (assumed to be perpendicular to the metal surface),  $\tilde{\mathbf{E}}_{\text{spp}}(\mathbf{r})$  is the plasmon mode, normalized such that  $\int \int [\epsilon \tilde{\mathbf{E}}_{\text{spp}}^2 - \mu_0 \tilde{\mathbf{H}}_{\text{spp}}^2] d^3\mathbf{r} = 1$ , and  $n$  is the refractive index of the cavity volume.

By adopting a classical description for the QD modeled as a classical point-like oscillator and by assuming that the coupling is due to a single dominant plasmon mode, it has been recently shown that the complex frequencies,  $\tilde{\omega}_-$  and  $\tilde{\omega}_+$ , of the hybrid eigenstates of the coupled system can be calculated analytically with the classical formula known for Hermitian cavities, provided that the real coupling strength is replaced by [8]

$$g^2 = \Omega^2 \left[ 1 - i \frac{\text{Im}(\tilde{V})}{\text{Re}(\tilde{V})} \right] \quad (5)$$

where  $\Omega$  is the usual Rabi frequency. In particular, this implies that once the plasmon mode  $\tilde{\mathbf{E}}_{\text{spp}}(\mathbf{r})$  is computed and normalized,  $\tilde{V}(\mathbf{r})$  is known for a dipole located at every point in space, and so maps of  $\tilde{\omega}_-$  and  $\tilde{\omega}_+$  are deduced analytically. We did not entirely follow this track in this paper, but instead confined ourselves to compute  $\tilde{V}$  map for several tip locations.

The maps of the complex mode volume for a unitary vector  $\mathbf{u}$  perpendicular to the substrate are computed using the same geometry as for the previous FEM calculations. The normalized eigenfield  $\tilde{\mathbf{E}}_{\text{spp}}(\mathbf{r})$  is obtained using the QNM solver QNMEig [9] implemented in COMSOL Multiphysics. This Comsol model is available on the web site of the Lalanne group [10]. The computation of each plasmon mode is performed in 2 min with a standard desktop computer, and its normalization is achieved by integrating over the full numerical space. From the normalized field

$\tilde{\mathbf{E}}_{\text{spp}}(\mathbf{r})$ , the mode volume, the Purcell factor, the coupling strength, and the new eigenfrequencies  $\tilde{\omega}_-$  and  $\tilde{\omega}_+$  can be computed analytically, see Eqs. (8.2) -(8.5) in [8], for any position of the oscillator.

We calculated and mapped both the real  $Re(V_{\text{cav}})$  and imaginary  $Im(V_{\text{cav}})$  contributions to the cavity mode volume for the entire plane of the cavity, as shown in Fig. S4. The imaginary contribution to the cavity mode volume was found to be negligible compared to the real part for all points in space, where the field enhancement is large (small  $Re(\tilde{V})$ ). We therefore consider only the real part of the complex mode volume in the main text.

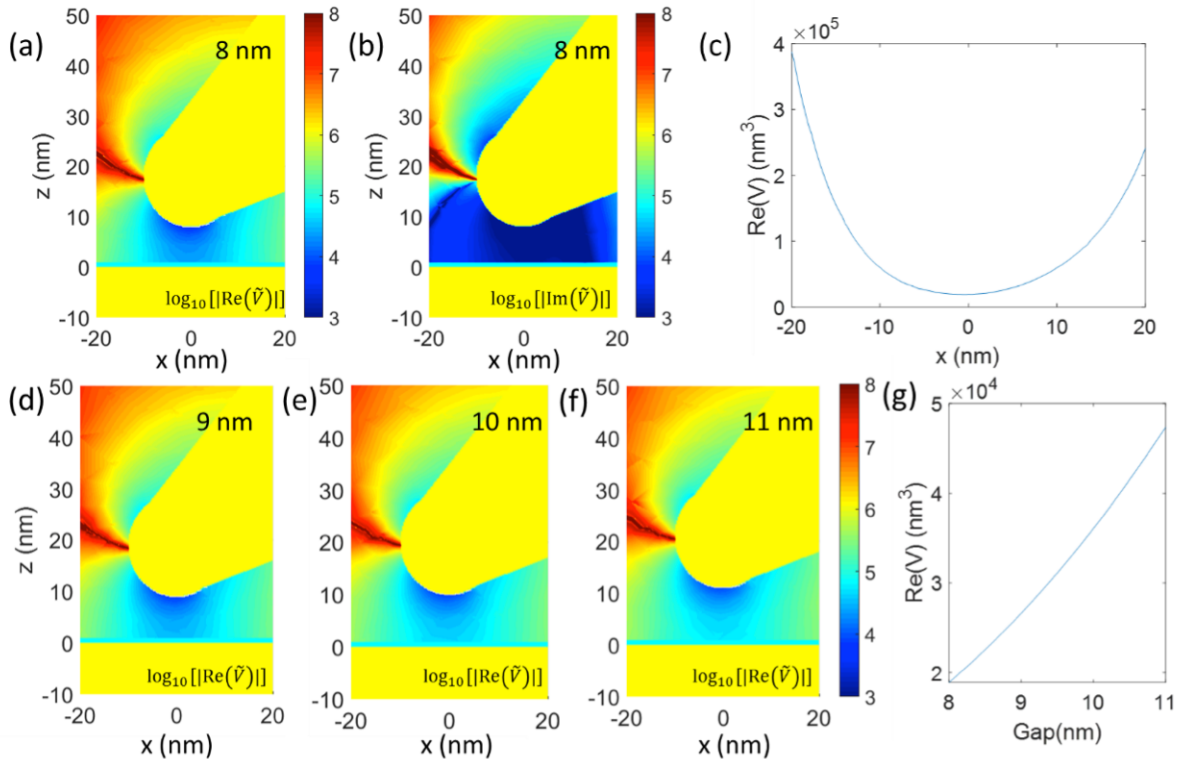


FIG. S4. **Theoretical modeling of mode volume.** (a-b) Maps of  $Re(\tilde{V})$  and  $Im(\tilde{V})$  for an 8-nm air gap. The Au substrate is covered by a 1-nm-thick  $\text{Al}_2\text{O}_3$  layer with ( $n_{\text{Al}_2\text{O}_3}=1.71$ ). The gold permittivity is approximated by a double-pole Drude-Lorentz model with  $\epsilon_\infty = 6$ ,  $\omega_{\text{spp}} = 5.37 \times 10^{15}$  rad/s,  $\omega_{\text{P}2} = \times 10^{15}$  rad/s,  $\gamma_{\text{spp}} = 6.216 \times 10^{13}$  rad/s,  $\gamma_{\text{P}2} = 1.332 \times 10^{15}$  rad/s,  $\omega_{01} = 0$  rad/s, and  $\omega_{02} = 4.572 \times 10^{15}$  rad/s. (c)  $Re(\tilde{V})$  at  $z = 4$  nm above the substrate as the lateral position  $x$  is varied (horizontal scan). (d-g)  $Re(\tilde{V})$  maps for 9, 10, 11-nm tip-substrate gap widths. (g)  $Re(\tilde{V})$  at  $(x,z)=(0,4)$  nm as a function of the gap width (vertical scan).

In future experiments, the finite size and dielectric behavior of the QD could be addressed by modeling the QD as a polarizability tensor of which elements are calculated from the QD's dipolar response. For a spherical QD of radius  $R$ , this takes the simple form of  $\alpha(\omega) = 4\pi R^3 \epsilon_b \epsilon_0 \left[ \frac{\epsilon_{\text{QD}}(\omega) - \epsilon_b}{\epsilon_{\text{QD}}(\omega) + 2\epsilon_b} \right] \bar{I}$  with  $\bar{I}$  being a three by three unit matrix and  $\epsilon_{\text{QD}}$  and  $\epsilon_b$  the permittivity of the quantum dot and background medium, respectively. The coupling strength can be computed analytically by solving a self-consistent equation that gives the induced dipole moment of the QD inside the cavity when the incident field is absent. The coupling strength can then be expressed as a function of the mode

volume of the cavity at the position of the QD.

As a second method, the QD could be modeled as an ensemble of evenly distributed Lorentz Dirac oscillators each possessing a polarizability of  $\alpha(\omega) = [\epsilon_{QD}(\omega) - \epsilon_{\infty}(\omega)] \frac{V}{N}$  with  $N$  being the number of the oscillators and  $V$  the volume of the resonator. Then if the couplings between different emitters are weak and can be ignored, the coupling strength can be calculated with  $(\sum_{i=1}^N \frac{V}{N} g(\mathbf{r}_i)^2)^{1/2}$  [11] where  $g(\mathbf{r}_i)$  is a local coupling for the  $i^{th}$  Lorentz Dirac emitter which can be calculated from Eq. (8.4) in ref. [8].  $g(\mathbf{r}_i)$  is determined by the mode volume at  $\mathbf{r}_i$ .

- [1] K. Karrai, R. D. Grober. *Appl. Phys. Lett.* **1995**, *66*, 14 1842.
- [2] K.-D. Park, M. B. Raschke. *Nano Lett.* **2018**, *18*, 5 2912.
- [3] G. Cui, M. G. Raymer. *Phys. Rev. A* **2006**, *73*, 5.
- [4] M. Pelton, D. Storm, H. Leng. *Nanoscale* **2019**.
- [5] X. Wu, S. K. Gray, M. Pelton. *Optics express* **2010**, *18*, 23 23633.
- [6] A. D. Raki, A. B. Djurii, J. M. Elazar, M. L. Majewski. *Applied Optics* **1998**, *37*, 22 5271.
- [7] C. Sauvan, J. P. Hugonin, I. S. Maksymov, P. Lalanne. *Physical Review Letters* **2013**, *110*, 23 237401.
- [8] P. Lalanne, W. Yan, K. Vynck, C. Sauvan, J.-P. Hugonin. *Laser & Photonics Reviews* **2018**, *12*, 5 1700113.
- [9] W. Yan, R. Faggiani, P. Lalanne. *Physical Review B* **2018**, *97*, 20 205422.
- [10] P. Lalanne. QNMEig and companion Matlab Toolboxes. URL <https://www.lp2n.institutoptique.fr/Membres-Services/Responsables-d-equipe/LALANNE-Philippe>.
- [11] C. Tserkezis, A. I. Fernandez-Domnguez, P. A. D. Goncalves, F. Todisco, J. D. Cox, K. Busch, N. Stenger, S. I. Bozhevolnyi, N. A. Mortensen, C. Wolff. *arXiv:1907.02605 [cond-mat, physics:physics, physics:quant-ph]* **2019**, arXiv: 1907.02605.